ARTICLE

Molecular Dynamics Study of OH-Induced Disintegration of Cu/ZnO Catalysts Based on Machine Learning Potentials

Junju Xue[a], Jianyu Hu[b], Jie Luo[a], Sulei Hu[b*], Wei-Xue Li[a,c*]

a. State Key Laboratory of Precision and Intelligent Chemistry, School of Chemistry and Materials Science, University of Science and Technology of China, Hefei 230026, China
b. Hefei National Research Center for Physical Sciences at the Microscale, University of Science and Technology of China, Hefei 230026, China
c. Hefei National Laboratory, University of Science and Technology of China, Hefei 230088, China

(Dated: Received on April 22, 2025; Accepted on June 3, 2025)

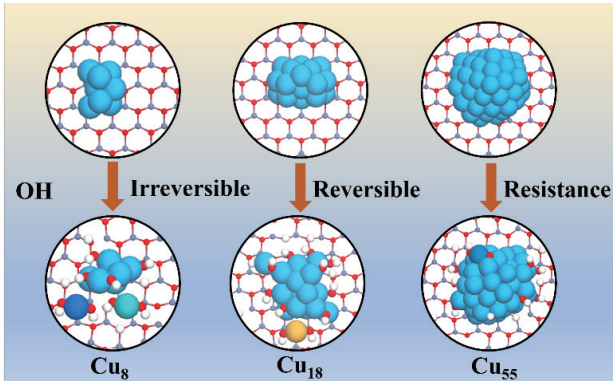

Supported metal catalysts have attracted significant attention in the field of heterogeneous catalysis due to their excellent catalytic performance and wide-ranging industrial applications. Among them, Cu/ZnO catalysts, as a typical supported metal system, exhibit outstanding activity in key industrial reactions such as the water-gas shift reaction (WGSR) and methanol synthesis. However, their stability under H_2O-rich conditions remains a critical issue that affects both the catalyst's long-term durability and catalytic efficiency. In this study, we investigate the thermodynamic stability and dynamic evolution of Cu/ZnO catalysts in the presence of H_2O using first principles calculation combined with molecular dynamics (MD) simulations based on machine learning potentials. Our results reveal that H_2O molecules can interact with isolated Cu atoms to form Cu–OH complexes, significantly lowering the formation energy of Cu single atoms on the ZnO($10\bar{1}0$) surface. Further MD simulations under given atmospheric and simulation conditions were performed. Small Cu clusters (Cu_8 and Cu_{18}) are more prone to forming $Cu(OH)_2$ complex, whereas no Cu–OH complexes are observed in larger clusters (Cu_{55}). This work elucidates the destabilizing role of water molecules on Cu/ZnO catalysts and deepens our understanding of their structural evolution under H_2O-rich environments. The findings provide valuable theoretical insights and data support for optimizing the stability of Cu/ZnO catalysts under reaction conditions.

Key words: Density functional theory, Machine learning potentials, Molecular dynamics simulation, Catalyst stability, Heterogeneous catalysis

I. INTRODUCTION

Heterogeneous catalysts play a vital role in energy conversion, environmental remediation, and chemical synthesis, driving sustainable industrial processes through enhanced reaction efficiency, selectivity, and stability. During catalytic reactions, strong interactions between metal atoms and supports, as well as between metal atoms and reactant molecules, can induce dynamic changes in the catalyst's geometric structure and chemical composition. These transformations in-

* Authors to whom correspondence should be addressed. husulei@ustc.edu.cn, wxli70@ustc.edu.cn

volve the formation of alloy phases [1, 2], oxide phases [3], or non-stoichiometric surface oxide layers [3], and so on. Supported metal nanoparticles, under reaction conditions, undergo sintering via particle migration and coalescence [4] or Ostwald ripening (OR) [5], or even disintegrate into smaller clusters or isolated single atoms [6, 7], ultimately resulting in catalyst deactivation. Capturing and understanding the dynamic behavior of catalysts under realistic reaction conditions is essential for elucidating catalytic mechanisms and improving catalyst performance. Although recent advances in characterization techniques have enabled the direct observation of catalyst evolution under reaction conditions [8], challenges persist in resolving dynamic structural evolution due to material-specific constraints and insufficient spatiotemporal resolution. Machine learning potentials (MLPs) now enable *ab initio*-accurate simulations of catalytic systems, bridging quantum-mechanical fidelity and mesoscopic spatiotemporal scales to resolve dynamic atomic rearrangements under operando conditions [9, 10].

Cu/ZnO heterogeneous catalysts, widely utilized in industrial processes such as CO/CO_2 hydrogenation to methanol [11, 12] and the water-gas shift reaction (WGSR) [13, 14], encounter significant durability challenges in aqueous environments. While advanced characterization techniques have clarified critical aspects—including active site electronic configurations [1, 15, 16], metal-support interaction mechanisms [3], degradation pathways [17], and advancements in synthetic methodologies [18]. The multiscale structural evolution of these catalysts under hydrothermal conditions remains a key efficiency constraint. The aqueous environment induces paradoxical catalytic effects: water promotes methanol synthesis through hydration of $*OCH_3$ intermediates [19]; however, it has also been reported to inhibit H_2 activation and CO_2 adsorption due to active site blocking [20]. These dual functionalities arise from water's capacity to act as both a reactive participant and structural modulator. Operando studies have identified H_2O-induced sintering, manifested as XRD-detectable crystalline growth, which collectively diminish active site availability and mass transport efficiency [17]. Interfacial restructuring under reactive atmospheres (*e.g.*, CO/H_2O) generates disordered CuO_x clusters on ZnO surfaces while expanding Cu-ZnO interfacial areas, indicative of water-enhanced metal-support interactions [3]. Spectroscopic investigations further reveal water's involvement in redox processes, including oxygen vacancy occupation at ZnO interfaces and Zn site reoxidation [21, 22], confirming its dynamic role in electronic and structural modifications. Crucially, under H_2/H_2O atmospheres, water adsorption dominates over gaseous reactants in driving Cu nanoparticle morphological evolution [23]. Notably, sintered Cu catalysts demonstrate room-temperature reactivation via O_2/H_2O-mediated oxidative-reductive cycling, overcoming traditional high-temperature dispersion constraints. In a humid O_2 environment, H_2O promotes the formation of hydroxylated Cu species and facilitates the migration of Cu atoms on γ-Al_2O_3 surfaces [6]. This discovery prompts critical questions regarding hydration-driven dispersion universality: can interfacial hydroxylation induce thermodynamic instability and kinetically accessible detachment pathways for Cu clusters on ZnO under moisture exposure? Resolving this demands concurrent analysis of hydration-mediated surface free energy modifications and hydroxyl-assisted bond cleavage dynamics at metal-support interfaces.

To systematically address these interfacial hydration mechanisms, we combine thermodynamic stability analysis with dynamic pathway interrogation. Density functional theory (DFT) calculations quantify the formation energetics of the isolated Cu–OH_x species ($x=0$, 2), comparing the disintegration free energy of Cu_n clusters ($n=8$, 18, 55) on ZnO($10\bar{1}0$). These calculations reveal an OH-induced thermodynamic preference shift from clustered to hydroxylated single-atom configurations. Complementarily, machine learning-accelerated MD simulations track hydroxyl-assisted bond cleavage dynamics across these three cluster sizes, establishing size-dependent disintegration stability. The multiscale results demonstrate two critical size-governed phenomena: (i) small subnano clusters (Cu_8) exhibit spontaneous hydroxyl adsorption initiating Cu–Cu bond rupture, while (ii) larger assemblies (Cu_{55}) maintain structural integrity—directly correlating thermodynamic instability with kinetically viable detachment mechanisms at the hydrated interface.

II. COMPUTATIONAL METHODS

All first-principles calculations were performed using the Vienna *Ab initio* Simulation Package (VASP) [24, 25], employing the projector augmented-wave (PAW) method [26] and the Perdew–Burke–Ernzerhof

DOI: 10.1063/1674-0068/cjcp2504046

(PBE) exchange–correlation functional [27] within the generalized gradient approximation (GGA) [28]. The plane-wave kinetic energy cutoff was set to 400 eV. Electronic self-consistency was achieved with a convergence threshold of 10^{-4} eV, and the force convergence threshold was set to 0.05 eV/Å. The PBE functional was used to optimize the bulk lattice constants of ZnO ($a=3.296$ Å, $c=5.279$ Å; experimental values: $a=3.250$ Å, $c=5.207$ Å [29]) and Cu (3.63 Å; experimental value: 3.62 Å [30]), yielding results in good agreement with experimental data. A (3×3) supercell of the ZnO($10\bar{1}0$) surface consisting of three atomic layers was constructed. During structural optimization, the bottom layer was fixed to represent the bulk structure, while the surface and adsorbates were fully relaxed. A 15 Å vacuum layer was introduced along the z-direction to eliminate spurious interactions between periodic images. Spin polarization was taken into account for both the surface and gas molecules. The effect of the Hubbard U correction was not considered in this study [31]. The climbing image nudged elastic band (CI-NEB) method [32, 33] was used to locate transition states, with a force convergence criterion of 0.05 eV/Å, and the uniqueness of the imaginary frequency was ensured to confirm true transition states.

MD simulations were performed using the Large scale Atomic Simulation with neural network Potential (LASP) software [10]. In this work, we used the first quinary Cu-Zn-C-O-H global neural network (G-NN) potential within the LASP software. The details of the method have been previously reported. The quality of the potential energy surface (PES) of G-NN is largely determined by its training dataset. To encompass all possible microenvironments of $Cu_x(OH)_y$ clusters on ZnO surface systems, SSW algorithm was employed to explore compositions, atom number per unit cell (~4–104) and various geometrical structures (including clusters, slab models, and bulk structures) based on 613 systems. The final training set comprised 63539 configurations calculated using highly accurate DFT, containing a variety of structural patterns on the global PES as summarized in Table S2 (Supplementary materials, SM). The first-principles method incorporated a plane-wave cutoff radius of 450 eV and an electronic step convergence criterion of 5×10^{-6} eV, using Gaussian smearing with a smearing width set to 0.05 eV. K-points were set to the gamma point for calculations involving meteorological clusters, whereas a fully automatic method grid was employed otherwise.

The stochastic surface walking (SSW) method [34, 35] was employed to explore the low-energy structural configurations of Cu particles of various sizes adsorbed on the ZnO($10\bar{1}0$) surface. These configurations were then used as initial structures for subsequent simulations. To identify the most representative catalyst structures under near-real reaction conditions, the grand canonical Monte Carlo (GCMC) method was applied. Based on the SSW-optimized configurations, GCMC simulations were performed for the Cu_8, Cu_{18}, Cu_{55}/ZnO($10\bar{1}0$) systems under WGSR reaction conditions (500 K, 1 bar H_2O partial pressure) [36]. The stable structures obtained from the GCMC simulations were used as the initial configurations for the subsequent MD simulations. MD simulations were carried out in the NVT ensemble at 500 K, with a time step of 1 fs and a total simulation duration of 1 ns. The ZnO surface was modeled using a (9×6) supercell with a 50 Å vacuum region along the z-direction to avoid periodic image interactions. To represent the bulk-like behavior of the support, atoms in the bottom layer were fixed during the simulation, while the top layers and adsorbates were allowed to fully relax to capture their dynamic evolution. The Cu–Cu nearest-neighbor distances were analyzed along the MD trajectories to investigate the size-dependent structural dynamics of the supported clusters under near-operando conditions.

In practical catalytic processes, supported metal nanoparticles often experience surface structural transformations in response to the surrounding reactive atmosphere, which may result in aging, sintering, or even disintegration [37]. Based on the stability theory for nanocatalysts under reaction conditions proposed by Li *et al.* [38–40], we can quantitatively describe the associated thermodynamic processes using first-principles calculation and machine learning potentials. The corresponding energy variations of supported catalysts in reactive environments are depicted in FIG. 1.

Compared to bulk materials (or infinite particles), the energy increase per atom in nanoparticles, $\Delta E_{\mathrm{NP}}(R)$, is given by:

$$\Delta E_{\mathrm{NP}}(R) = \frac{1}{y}\left(E_{\mathrm{sup+Cu}} - E_{\mathrm{sup}}\right) - \frac{1}{n}\cdot E_{\mathrm{bulk}} \qquad (1)$$

where $E_{\mathrm{sup+Cu}}$ denotes the total energy of the support surface with Cu nanoparticles loaded, E_{sup} is the total energy of the pristine support surface, E_{bulk} represents

DOI: 10.1063/1674-0068/cjcp2504046

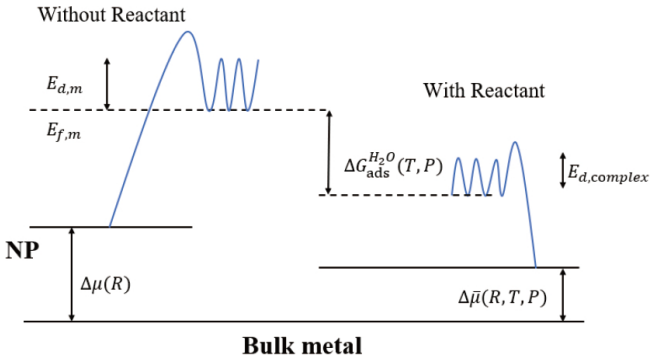

FIG. 1 Energy diagram of supported nanoparticles and surface single atom under reaction atmosphere.

the energy of bulk metal Cu, and y is the number of Cu atoms in the nanoparticles, while n denotes the number of Cu atoms in the bulk metal.

The total energy of a single Cu atom adsorbed on the support surface is represented by E_{ox}^{Cu}. The formation energy of a Cu single atom on the ZnO surface, E_f^{Cu}, is calculated as:

$$E_f^{Cu} = E_{ox}^{Cu} - E_{sup} - \frac{1}{n}E_{bulk} \tag{2}$$

The total energy of a Cu single-atom hydroxide complex adsorbed on the support surface is $E_{ox}^{Cu(OH)_x}$. The formation energy of $Cu(OH)_x$ (where x=1, 2) on the ZnO surface is given by:

$$\begin{aligned} E_f^{Cu(OH)_x} =& E_{ox}^{Cu(OH)_x} + x\cdot E_{H\text{-}sup} - x\cdot E_{H_2O} \\ & - (1+x)\cdot E_{sup} - \frac{1}{n}E_{bulk} \end{aligned} \tag{3}$$

where $E_{H\text{-}sup}$ is the total energy of hydrogen adsorbed on the surface oxygen species, E_{H_2O} denotes the energy of a gas-phase H_2O molecule. The total activation energy E_{tot} is expressed as:

$$E_{tot} = E_f^m + E_d^m \tag{4}$$

where E_f^m and E_d^m represent the formation energy and diffusion energy barrier of the Cu single atom or $Cu(OH)_x$ (where x=1, 2) complex on the surface, respectively. The adsorption energy of H_2O is calculated as:

$$\begin{aligned} E_{ad}^{H_2O} =& E_{ox}^{Cu(OH)_x} + x\cdot E_{H\text{-}sup} - E_{ox}^{Cu} \\ & - x\cdot E_{H_2O} - x\cdot E_{sup} \end{aligned} \tag{5}$$

To assess whether H_2O facilitates the disintegration of Cu nanoparticles, the Gibbs free energy of disintegration, ΔG_{NP}^{dis}, is employed. When $\Delta G_{NP}^{dis} < 0$, the particle is disintegrated; when $\Delta G_{NP}^{dis} > 0$, the particle is unlikely to disintegrate. The calculation formula is:

$$\Delta G_{NP}^{dis} = E_f^{Cu(OH)_x} - x\cdot\Delta\mu_{H_2O}(T,P) - \Delta E_{NP}(R) - TS \tag{6}$$

where S is the configurational entropy. Assuming a surface coverage of 0.01, the configurational entropy contribution is approximated as 4.83×10^{-4} T (in eV) [41].

TABLE I Formation energies of Cu, Cu(OH), and $Cu(OH)_2$ on the ZnO($10\bar{1}0$) surface, along with the corresponding diffusion energy barriers and the adsorption energy of H_2O on the Cu single atom (energy unit is eV).

Form. energy		Ads. energy		Diffusion energy	
E_f^{Cu}	1.36	$E_{ad}^{H_2O}(Cu(OH))$	−1.78	E_d^{Cu}	0.45
$E_f^{Cu(OH)}$	−0.42	$E_{ad}^{H_2O}(Cu(OH)_2)$	−2.46	$E_d^{Cu(OH)}$	0.60
$E_f^{Cu(OH)_2}$	−1.10			$E_d^{Cu(OH)_2}$	0.55

III. RESULTS AND DISCUSSION

A. Thermodynamic calculations of OH-induced disintegration of Cu particles on ZnO

To understand the stability of isolated Cu atoms on ZnO surface, we first evaluated their formation energy at the most stable adsorption site on ZnO($10\bar{1}0$), which is calculated to be 1.36 eV (Table I), indicating a significantly endothermic process. This suggests that single Cu atoms on ZnO($10\bar{1}0$) are thermodynamically unstable, leading to low surface concentrations and a strong tendency toward aggregation. However, when H_2O is introduced into the system, a strong interaction occurs between OH and the surface Cu single atoms, leading to the formation of a single-hydroxyl Cu complex (FIG. 2(b)), with an adsorption energy of −1.78 eV. Furthermore, a second OH can further adsorb on the Cu single atom, forming a bidentate Cu-hydroxide complex (FIG. 2(c)) with a total adsorption energy of −2.46 eV. Relative to bulk Cu, the formation energies of the Cu hydroxide complexes are −0.42 eV (single hydroxyl) and −1.10 eV (bidentate hydroxyl), indicating that OH adsorption significantly stabilizes the surface Cu single atoms.

For OR process, while pristine Cu nanoparticles exhibit a high total activation barrier (1.81 eV), hydroxyl coordination dramatically reduces the thresholds to 0.18 eV (Cu(OH)) and −0.55 eV ($Cu(OH)_2$)—a 10-fold decrease enabling spontaneous disintegration and fol-

DOI: 10.1063/1674-0068/cjcp2504046

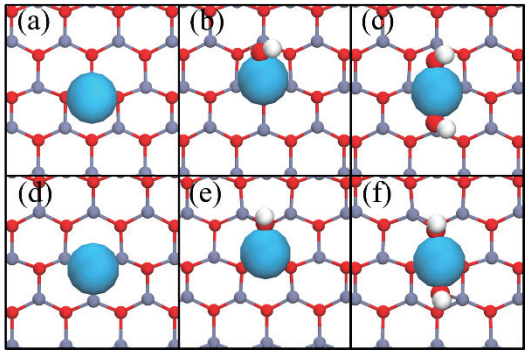

FIG. 2 Stable adsorption structures of (a) Cu, (b) Cu(OH), and (c) $Cu(OH)_2$ on the $ZnO(10\bar{1}0)$ surface, and (d–e) their corresponding transition state structures. Red: O; gray: Zn; blue: Cu; white: H.

lowing OR under hydration. However, the ultimate ripening propensity depends critically on two competing factors. (i) Transport efficiency: low diffusion barriers (≈ 0.5 eV) promote hydroxylated species migration toward larger clusters. (ii) Reintegration likelihood: energy cost for $Cu(OH)_x$ ($x=1$, 2) dissociation from stable clusters determines atomic reincorporation rates. Our data resolve the first factor but leave the second unexplored— the thermodynamic stability of mobile $Cu(OH)_x$ ($x=1$, 2) species upon encountering larger clusters remains unquantified. This knowledge gap prevents definitive ripening predictions, as fast transport (promoting ripening) could be counterbalanced by strong $Cu(OH)_x$–cluster binding (inhibiting atomic release). Future work must probe $Cu(OH)_x$/cluster interfacial energetics to establish whether hydration ultimately accelerates sintering or enables size-stabilized dispersion.

B. Gibbs free energy of disintegration

The stable structures of $ZnO(10\bar{1}0)$-supported Cu_8, Cu_{18}, and Cu_{55} clusters were systematically mapped based on the SSW method. We computed ΔG_{NP}^{dis} for clusters disintegration into hydroxylated Cu–OH_x species ($x=1$, 2) across temperature (300–1000 K) ranges and H_2O partial pressures (10^{-4} and 1 bar), as quantified in the phase diagrams of FIG. 3(a–c). Three critical trends emerge: (i) all systems exhibit linear $\Delta G_{NP}^{dis} \propto T$ relationships, demonstrating enhanced thermodynamic driving forces for cluster disintegration at lower temperatures. The $Cu(OH)_2$ pathway shows steeper slopes ($\Delta G_{NP}^{dis}/T$) compared to Cu(OH), attributable to its higher hydroxyl coordination enhancing entropy-driven stabilization. (ii) At 10^{-4} bar H_2O

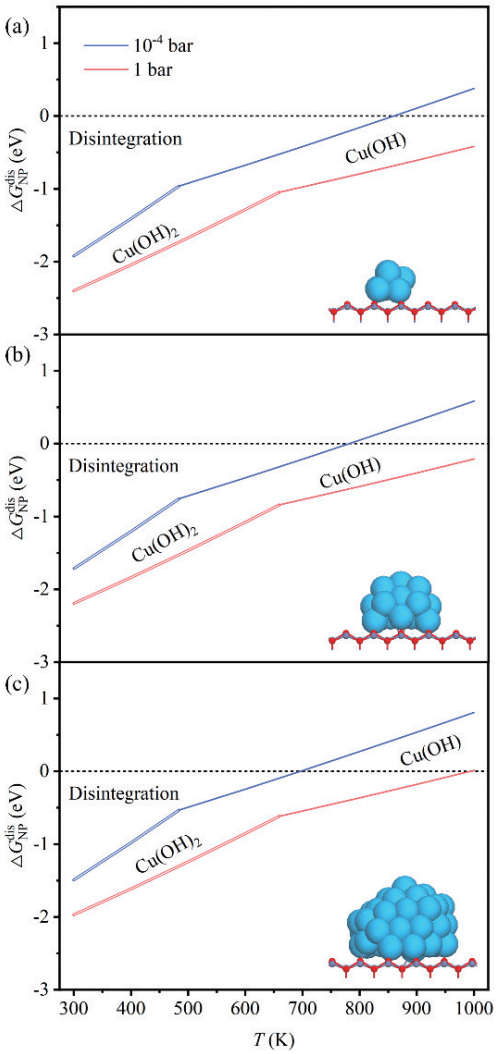

FIG. 3 Dependence of the disintegration Gibbs free energy of Cu(OH) (single solid line) and $Cu(OH)_2$ (double solid line) complexes on temperature, pressure, and Cu cluster size on the $ZnO(10\bar{1}0)$ surface, along with the corresponding cluster structures. (a) $Cu_8/ZnO(10\bar{1}0)$, (b) $Cu_{18}/ZnO(10\bar{1}0)$, (c) $Cu_{55}/ZnO(10\bar{1}0)$. Red: O; gray: Zn; blue: Cu.

pressure (FIG. 3 blue boundaries), $Cu(OH)_2$ dominates below 484 K (the intersection point between the blue double solid line and the blue single solid line), transitioning to Cu(OH) at higher temperatures. Elevated pressure (1 bar, red boundaries) shifts this threshold to 660 K, extending the $Cu(OH)_2$ stability domain by 176 K. Furthermore, increasing the H_2O pressure leads to a reduction in ΔG_{NP}^{dis}, highlighting the role of water in promoting the disintegration of Cu clusters into hydroxylated species. (iii) With increasing particle size, the temperature window for which $\Delta G_{NP}^{dis} < 0$ becomes narrower, reflecting the enhanced thermodynamic stability of larger particles. Specifically, under 10^{-4} bar

DOI: 10.1063/1674-0068/cjcp2504046

conditions, Cu_8, Cu_{18}, and Cu_{55} clusters are thermodynamically favorable for disintegration into Cu–OH_x complexes ($x=1$, 2) below 850 K, 780 K, and 700 K (*i.e.*, the temperatures at which the corresponding ΔG_{NP}^{dis} curves intersect with the $\Delta G_{NP}^{dis}=0$ line), respectively. These results suggest that smaller clusters have lower thermodynamic stability and are more likely to undergo disintegration over a wider range of conditions.

Notably, under WGSR experimental conditions, all systems exhibit negative ΔG_{NP}^{dis} values favoring disintegration, with $Cu(OH)_2$ being energetically preferred. This establishes a clear thermodynamic hierarchy: smaller clusters and higher hydroxylation degrees synergistically drive metal dispersion.

C. Hydration-driven structural dynamics from bond-length evolution

1. Cu_8 cluster: deformation and irreversible detachment in water

To resolve the atomistic mechanisms of water-mediated cluster disintegration, we tracked the Cu–Cu nearest-neighbor distance evolution through combined MD simulations (FIG. 4). Under dry conditions (500 K), the Cu_8 cluster maintains robust structural integrity with Cu–Cu bond lengths tightly constrained within 2.2–2.4 Å over 1 ns simulation (FIG. 4(a)). The negligible bond-length variation across all atoms confirms a rigid metallic configuration.

Under H_2O-rich conditions (500 K and 1 bar H_2O partial pressure), GCMC simulations were performed based on the assumption that water readily dissociates at the Cu–ZnO interface [16, 42–44]. In the resulting stable structures, OH adsorbs on the Cu particle, while H adsorbs on the support surface, consistent with previous studies [16]. Initial stage (0–500 ps): OH preferentially adsorbs on edge Cu atoms, increasing surface bond-length dispersion (2.2–2.8 Å) while compressing the cluster into a flattened morphology, indicating enhanced metal-support interactions. About 600 ps: a boundary Cu atom (FIG. 4(b) blue trace) undergoes hydroxyl-assisted extraction, with its Cu–Cu bonds elongating abruptly to 3.6 Å—surpassing metallic bonding limits. This forms a $Cu(OH)_2$ complex anchored through dual Cu–O–Zn linkages. About 800 ps: adjacent Cu atoms (green trace) detach irreversibly ($d_{Cu-Cu}>4.0$ Å), forming secondary $Cu(OH)_2$ species.

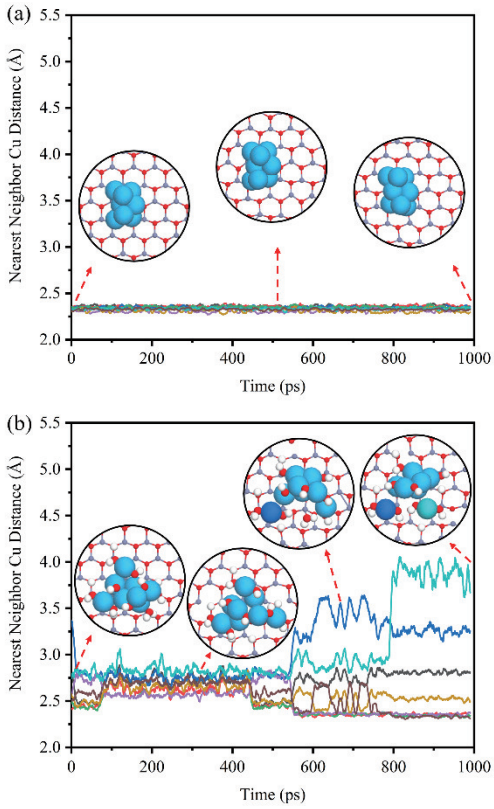

FIG. 4 (a) Cu–Cu nearest-neighbor distance analysis for $Cu_8/ZnO(10\bar{1}0)$ and (b) $Cu_8(H_2O)_9/ZnO(10\bar{1}0)$ with corresponding structural snapshots. Red: O; gray: Zn; blue, dark blue, green: Cu; white: H.

These hydroxylated complexes exhibit no reintegration tendencies after their formation due to stronger Cu–OH covalent bonding, demonstrating kinetic stabilization under operational hydration conditions.

2. Cu_{18} cluster: flattening and reversible detachment in water

Under dry conditions at 500 K (FIG. 5(a)), the Cu_{18} cluster maintains strong metallic cohesion, with the Cu–Cu nearest-neighbor distance fluctuating between 2.2 Å and 2.5 Å. Minor bond-length fluctuations are solely due to thermal vibrations, with the structure maintaining its integrity. This inherent stability disappears when introducing H_2O (1 bar), which induces significant structural transformations (FIG. 5(b)).

During the initial stage (0–200 ps), the Cu–Cu nearest-neighbor distance is mainly concentrated between 2.2 Å and 2.8 Å, indicating that the initial structure of the cluster remains relatively stable. However, compared to the cluster in the absence of H_2O, the distance distribution becomes more dispersed, suggesting that the adsorption of H_2O slightly elongates the Cu–Cu

DOI: 10.1063/1674-0068/cjcp2504046

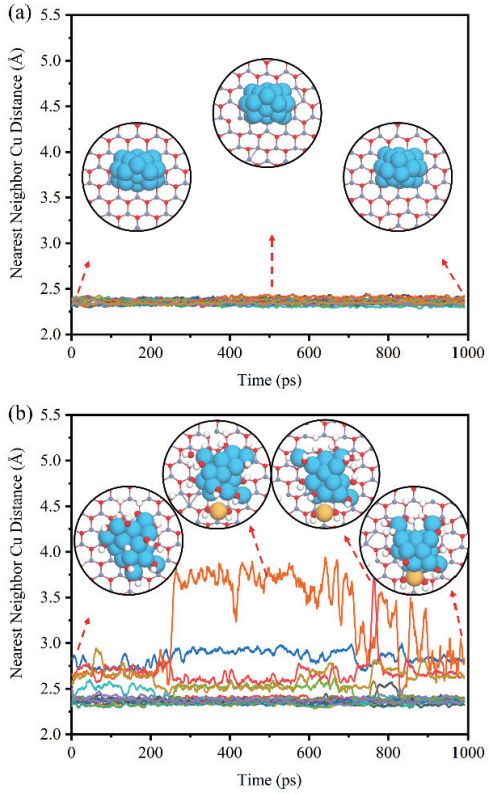

FIG. 5 (a) Cu–Cu nearest-neighbor distance analysis for $Cu_{18}/ZnO(10\bar{1}0)$ and (b) $Cu_{18}(H_2O)_{12}/ZnO(10\bar{1}0)$ with corresponding structural snapshots. Red: O; gray: Zn; blue, yellow: Cu; white: H.

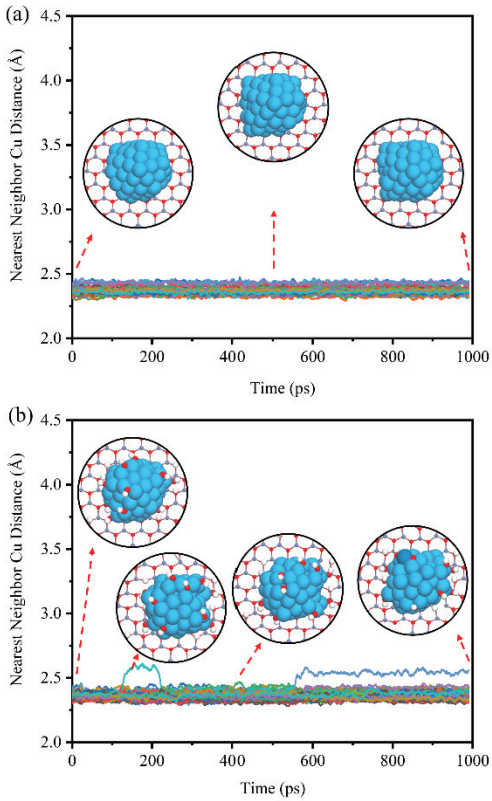

FIG. 6 (a) Cu–Cu nearest-neighbor distance analysis for $Cu_{55}/ZnO(10\bar{1}0)$ and (b) $Cu_{55}(H_2O)_{11}/ZnO(10\bar{1}0)$ with corresponding structural snapshots. Red: O; gray: Zn; blue, green, dark blue: Cu; white: H.

bond, weakening the interaction between Cu atoms. Concurrently, the hydrated environment induces significant nanoparticle morphological changes: compared to the hemispherical anhydrous configuration, the hydrated cluster becomes more flattened, indicating enhanced metal-support interaction. Around 250 ps, accumulated hydroxylation overcomes interfacial cohesion, extracting a boundary Cu atom (bond length 3.6 Å) into a $Cu(OH)_2$ complex. It is noteworthy that this complex remains stably present for approximately 600 ps before merging back with the original cluster, indicating that the $Cu(OH)_2$ complex possesses appreciable kinetic stability. This reversible restructuring behavior suggests that H_2O enables the formation and subsequent re-association of $Cu(OH)_2$ complexes, thereby dynamically modulating cluster integrity at the atomic level.

3. Cu_{55} cluster: stability and resistance to water-induced changes

The variation of Cu–Cu nearest-neighbor bond lengths during the simulation of Cu_{55} clusters on the $ZnO(10\bar{1}0)$ surface is presented in FIG. 6. In contrast to the evolution trends observed for Cu_8 and Cu_{18} clusters, Cu_{55} clusters exhibit distinctly different behavior. Regardless of the presence of H_2O, the Cu–Cu nearest-neighbor bond lengths fluctuate within a relatively stable range of 2.2 Å to 2.6 Å, which is consistent with typical bonding distances for metallic Cu. This stability suggests that, throughout the simulation, the Cu atoms remain firmly bound within the cluster, without undergoing significant structural reconstruction or dissociation into single-atom species.

FIG. 6 (a and b) illustrate the dynamic evolution of the Cu_{55} cluster on the $ZnO(10\bar{1}0)$ surface, in the absence and presence of H_2O, respectively. It is clear that the Cu_{55} cluster does not undergo substantial changes during the simulation, only exhibiting minor local thermal motion (FIG. 6(a)). Under H_2O-rich conditions (FIG. 6(b)), slight increases in Cu–Cu bond lengths are observed for certain atoms—such as the dark blue and green Cu atoms—but these values remain below 2.6 Å. This behavior suggests that larger clusters are kinetically more resistant to water-induced disintegration, in stark contrast to the dynamic restructuring observed in

DOI: 10.1063/1674-0068/cjcp2504046

smaller clusters. Thus, the introduction of H_2O leads to minimal structural changes, with no observed atom detachment, further highlighting the stability of larger Cu clusters under such conditions.

In summary, on the ZnO($10\bar{1}0$) surface, the adsorption of OH weakens the Cu–Cu interactions within Cu clusters across all investigated sizes, as evidenced by the elongation of Cu–Cu bond lengths. Additionally, after OH adsorption, the cluster structure becomes more expanded and flattened, indicating enhanced metal-support interactions. The extent of OH-induced structural deformation is strongly size-dependent. Smaller Cu particles (*e.g.*, Cu_8 and Cu_{18} clusters) show a more pronounced effect from OH, with clear structural changes, including the formation of Cu single-atom hydroxide complexes ($Cu(OH)_2$). In contrast, for larger Cu particles (*e.g.*, Cu_{55} clusters), the effect of OH is weaker, and the cluster structures with and without OH adsorption are similar. No Cu single-atom hydroxide complexes are observed, indicating that Cu–Cu interactions still dominate in larger Cu particles, leading to higher stability. This enhanced stability arises from their lower surface energy and higher coordination of surface atoms, which reduce their reactivity toward water and suppress the formation of hydroxylated species. Moreover, the formed Cu single-atom complexes are able to remain stable over a certain timescale, suggesting that they exhibit high kinetic stability.

IV. CONCLUSION

In this study, we systematically investigated the thermodynamic stability and dynamic evolution of Cu/ZnO catalysts in the presence of H_2O. Using DFT calculations, machine learning potential-based molecular dynamics simulations, and trajectory analysis, we reached the following conclusions:

(i) A single Cu atom supported on the ZnO($10\bar{1}0$) surface is inherently thermodynamically unstable. However, when H_2O (OH) is introduced into the system, OH can coordinate with the Cu single atom to form a single-atom Cu–OH_x complexes ($x=1$, 2), significantly reducing its formation energy and stabilizing the surface single atom. Phase diagram analyses further reveal that increasing the chemical potential of H_2O (*i.e.*, by decreasing temperature or increasing pressure) enhances the thermodynamic driving force for cluster disintegration. This effect is strongly size-dependent: smaller Cu clusters (*e.g.*, Cu_8 and Cu_{18}) exhibit a greater tendency to dissociate into hydroxylated single-atom species than larger clusters (*e.g.*, Cu_{55}), indicating that particle size plays a critical role in determining thermodynamic stability under aqueous conditions.

(ii) The adsorption of OH on Cu particles weakens Cu–Cu metallic bonds, as evidenced by the elongation of nearest-neighbor distances and structural deformation of the clusters. Upon OH adsorption, the clusters undergo expansion and flattening, reflecting enhanced metal–support interactions. The extent of this deformation is also size-dependent: small clusters display more pronounced local restructuring, and in some cases, extraction of individual Cu atoms to form stable $Cu(OH)_2$ complexes. In contrast, large clusters maintain their metallic bonding network and exhibit limited structural response. Notably, once formed, $Cu(OH)_2$ species demonstrate high kinetic stability and persist throughout the MD simulation, highlighting the ability of H_2O to facilitate yet kinetically favorable single-atom formation.

Our study reveals that under H_2O-involved conditions, the structural morphology of Cu in the Cu/ZnO system may transition from nanoparticles to single-atom Cu–OH complexes. This phenomenon is significant for understanding the stability of Cu/ZnO catalysts. The results not only enhance the understanding of the dispersion behavior of Cu on ZnO support but also provide data support for the subsequent optimization of Cu/ZnO catalysts. In the future, additional experiments are needed to further validate these findings and provide more comprehensive insights.

Supplementary materials: Energy comparison between LASP and DFT, types of structures used for potential training, other calculated configurations, selection of U-values and functionals and radial distribution function calculations.

V. ACKNOWLEDGMENTS

This work was supported by the National Natural Science Foundation of China (Nos. 22221003, 22173058, 22372153), the Strategic Priority Research Program of the Chinese Academy of Sciences (XDB0450102), Innovation Program for Quantum Science and Technology (2021ZD0303302), Anhui Outstanding Youth Fund (2208085J27), National Program for Support of Top-notch Young Professional, Chinese Academy of Sci-

ences Youth Innovation Promotion Association, the Fundamental Research Funds for the Central Universities (20720220009), USTC Research Funds of the Double First-Class Initiative. The AI-driven experiments, simulations and model training were performed on the robotic AI-Scientist platform of Chinese Academy of Science. The authors thank Supercomputing Center of University of Science and Technology of China and Hefei Advanced Computing Center.

[1] M. Behrens, F. Studt, I. Kasatkin, S. Kühl, M. Hävecker, F. Abild-Pedersen, S. Zander, F. Girgsdies, P. Kurr, B. L. Kniep, M. Tovar, R. W. Fischer, J. K. Nørskov, and R. Schlögl, Science **336**, 893 (2012).
[2] F. Tao, M. E. Grass, Y. W. Zhang, D. R. Butcher, J. R. Renzas, Z. Liu, J. Y. Chung, B. S. Mun, M. Salmeron, and G. A. Somorjai, Science **322**, 932 (2008).
[3] Z. Dong, W. Liu, L. Zhang, S. Wang, and L. Luo, ACS Appl. Mater. Interfaces **13**, 41707 (2021).
[4] E. M. Dietze, F. Abild-Pedersen, and P. N. Plessow, J. Phys. Chem. C **122**, 26563 (2018).
[5] Q. Wan, F. Wei, Y. Wang, F. Wang, L. Zhou, S. Lin, D. Xie, and H. Guo, Nanoscale **10**, 17893 (2018).
[6] Y. M. Fan, R. T. Li, B. B. Wang, X. Feng, X. Du, C. Liu, F. Wang, C. Liu, C. Dong, Y. Ning, R. Mu, and Q. Fu, Nat. Commun. **15**, 3046 (2024).
[7] C. Chen, J. L. Chen, L. Feng, J. Hu, X. Chai, J. X. Liu, and W. X. Li, ACS Catalysis **14**, 3504 (2024).
[8] S. W. Chee, T. Lunkenbein, R. Schlögl, and B. R. Cuenya, J. Phys.: Condens. Matter **33**, 153001 (2021).
[9] H. Wang, L. Zhang, J. Han, and W. E, Comput. Phys. Commun. **228**, 178 (2018).
[10] S. D. Huang, C. Shang, P. L. Kang, X. J. Zhang, and Z. P. Liu, Wiley Interdiscip. Rev. Comput. Mol. Sci. **9**, (2019).
[11] A. Y. Rozovskii and G. I. Lin, Top. Catal. **22**, 137 (2003).
[12] G. Pacchioni, ACS Catalysis **14**, 2730 (2024).
[13] L. C. Grabow, A. A. Gokhale, S. T. Evans, J. A. Dumesic, and M. Mavrikakis, J. Phys. Chem. C **112**, 4608 (2008).
[14] E. Baraj, K. Ciahotný, and T. Hlinčík, Fuel **288**, 119817 (2021).
[15] S. Kattel, P. J. Ramírez, J. G. Chen, J. A. Rodriguez, and P. Liu, Science **355**, 1296 (2017).
[16] Z. Zhang, X. Chen, J. Kang, Z. Yu, J. Tian, Z. Gong, A. Jia, R. You, K. Qian, S. He, B. Teng, Y. Cui, Y. Wang, W. Zhang, and W. Huang, Nat. Commun. **12**, 4331 (2021).
[17] J. Wu, M. Saito, M. Takeuchi, and T. Watanabe, Appl. Catal. A Gen. **218**, 235 (2001).
[18] H. Yang, P. Gao, C. Zhang, L. Zhong, X. Li, S. Wang, H. Wang, W. Wei, and Y. Sun, Catal. Commun. **84**, 56 (2016).
[19] Y. H. Wang, W. G. Gao, K. Z. Li, Y. Zheng, Z. Xie, W. Na, J. G. Chen, and H. Wang, Chemistry **6**, 419 (2020).
[20] K. Klier, V. Chatikavanij, R. G. Herman, and G. W. Simmons, J. Catal. **74**, 343 (1982).
[21] M. Kurtz, J. Strunk, O. Hinrichsen, M. Muhler, K. Fink, B. Meyer, and C. Wöll, Angew. Chem., Int. Ed. **44**, 2790 (2005).
[22] S. Kuld, C. Conradsen, P. G. Moses, I. Chorkendorff, and J. Sehested, Angew. Chem., Int. Ed. **53**, 5941 (2014).
[23] P. L. Hansen, J. B. Wagner, S. Helveg, J. R. Rostrup-Nielsen, B. S. Clausen, and H. Topsøe, Science **295**, 2053 (2002).
[24] G. Kresse and J . Furthmüller, Comput. Mater. Sci. **6**, 15 (1996).
[25] G. Kresse and J. Furthmüller, Phys. Rev. B **54**, 11169 (1996).
[26] G. Kresse and D. Joubert, Phys. Rev. B **59**, 1758 (1999).
[27] John P. Perdew, Kieron Burke, and M. Ernzerhof, Phys. Rev. Lett. **77**, 3865 (1996).
[28] D. C. Langreth and J. P. Perdew, Solid State Commun. **31**, 567 (1979).
[29] J. Sołtys, J. Piechota, M. Łopuszyński, and S. Krukowski, J. Cryst. Growth **374**, 53 (2013).
[30] S. Peljhan and A. Kokalj, Phys. Chem. Chem. Phys. **13**, 20408 (2011).
[31] X. K. Gu, B. T Qiao, C. Q. Huang, W. C. Ding, K. Sun, E. Zhan, T. Zhang, J. Liu, and W. X. Li, ACS Catalysis **4**, 3886 (2014).
[32] G. Henkelman and H. Jónsson, J. Chem. Phys. **113**, 9978 (2000).
[33] G. Henkelman, B. P. Uberuaga, and H. Jónsson, J. Chem. Phys. **113**, 9901 (2000).
[34] C. Shang and Z. P. Liu, J. Chem. Theory Comput. **9**, 1838 (2013).
[35] C. Shang, X. J. Zhang, and Z. P. Liu, Phys. Chem. Chem. Phys. **16**, 17845 (2014).
[36] C. Price, L. Pastor-Pérez, E. le Saché, A. Sepúlveda-Escribano, and T. R. Reina, Int. J. Hydrogen Energy **42**, 10747 (2017).
[37] X. y. Duan, Y. Han, B. E. Zhu, and Y. Gao, Mater. Today Catal. **3**, 100032 (2023).
[38] R. Ouyang, J. X. Liu, and W. X. Li, J. Am. Chem. Soc. **135**, 1760 (2013).
[39] S. Hu and W. X. Li, Science **374**, 1360 (2021).
[40] S. Y. Cao, S. L. Hu, and W. X. Li, Chin. J. Chem. Phys. **36**, 411 (2023).
[41] K. Reuter and M. Scheffler, Phys. Rev. B **68**, 045407 (2003).
[42] B. Meyer, H. Rabaa, and D. Marx, Phys. Chem. Chem. Phys. **8**, 1513 (2006).
[43] V. T. Cong, L. K. Huynh, J. C. Jiang, N. T. A. Nhung, and P. V. Tat, Comput. Theor. Chem. **1081**, 62 (2016).
[44] A. A. Gokhale, J. A. Dumesic, and M. Mavrikakis, J. Am. Chem. Soc. **130**, 1402 (2008).

DOI: 10.1063/1674-0068/cjcp2504046